Molecule Binding Parameter Estimation from Surface Plasmon Resonance Measurements

Yanjun Yan, Le Chen, Peter C. Tay, and Martin L. Tanaka
College of Engineering + Technology
Western Carolina University
Cullowhee, NC 28723, USA
yyan@wcu.edu

***Abstract*—Surface Plasmon Resonance (SPR) is a highly sensitive technique that utilizes the properties of surface plasmons to detect the subtle changes in mass caused by adsorption of molecules. The SPR technique is appealing because the amount of adsorption is detected in real time, without the need to label the adsorbate or prepare samples using a complex procedure. Although much progress has been made in the analysis of SPR images several challenges remain. In this paper, we addressed two of these challenges, 1) automatic detection of regions of interest (ROIs) and 2) accurate estimation of the molecular association and disassociation parameters. With hundreds of ROIs on a single SPR video frame image, our procedure to automatically detect the ROIs greatly reduces the labor and time. The gray level values of the ROIs were extracted over time and used to estimate the molecule binding parameters, which are vital in biosensing applications. The parameters were estimated using Particle Swarm Optimization (PSO) and the standard Levenberg-Marquardt (LM) algorithm. A comparison of the results revealed that the PSO algorithm achieved a much lower mean squared error (MSE), and hence more accurate, than the LM algorithm for all of the active ROIs.**

***Index Terms*—urface Plasmon Resonance (SPR), Image Analysis, Absorption, Particle Swarm Optimization, Estimationurface Plasmon Resonance (SPR), Image Analysis, Absorption, Particle Swarm Optimization, EstimationS**

I. Introduction

Biomolecular interaction analysis is used to understand what happens when different molecules encounter each other. This knowledge is crucial for the advancement of biomedical research and the development of medication in the pharmaceutical industry. An understanding of molecular binding properties is necessary when determining the choice of drug target [1], [2] or developing critical antibodies [3]. Many analytical techniques have been designed to study biomolecular interactions, such as scanning probe microscopy (SPM) [4], attenuated total reflectance infrared spectroscopy (ATR-IR) [5] and spectral ellipsometry [6]. However, these techniques cannot perform analysis in real-time and are not sensitive enough for many applications in life science research.

Surface plasmons are electro-magnetic waves that propagate along the interface between a metal and a dielectric material under certain conditions. Surface Plasmon Resonance (SPR) [7] has attracted considerable interest in bio-analytical research, environment monitoring, and food safety applications [8], [9], [10] because it is highly sensitive, does not require the analyte to be labeled, and can be processed in real time.

Various techniques have been proposed to enhance SPR sensing efficiency and accuracy, such as using a high-performance metal and dielectric interface layer [11], applying a more stable protein adhesion site [12], and designing a different structure of SPR devices for sensing [13]. These approaches have greatly improved SPR sensing capability and the detection results. However, there has been little work on employing data processing techniques to optimize the post-processing of SPR measurements. In practice, the ROIs are often located manually, which is costly both in labor and processing time. Hence, the first goal of this paper is to develop an image processing based procedure to automatically detect the ROIs. The second goal of this paper is to accurately estimate the molecule association and dissociation parameters. The LM algorithm is commercially implemented and considered to be the state of the art algorithm in SPR measurements. However, the LM algorithm is gradient based and susceptible to falling into a local minimum. On the other hand, the PSO algorithm is a bottom-up random search algorithm, which can effectively avoid local minima. In this paper, PSO will be evaluated to determine if it can achieve better fitting results than the LM algorithm.

The rest of the paper is organized as follows. Section II provides a brief overview of the SPR technique and its sensorgram data. Section III describes the image processing technique for ROI detection. Section IV explains the application of PSO to estimate the molecule binding kinetic parameters. Section V presents the results. Section VI concludes this paper and includes future work.

II. Background

A. Surface plasmon resonance

In SPR, a p-polarized (polarized in the plane of the surface) and collimated light beam is passed through the surface between the prism and a glass slide coated with gold (or other metal). The light is reflected off the thin gold coating (with a thickness in the range of nm) that is in contact with the liquid solution of interest. At the interface between the gold and the solution, the incident light beam excites electron waves, which are called surface plasmons.

At a certain incident angle, excitation of the surface plasmons results in nearly complete attenuation of the specularly reflected light intensity, thus reducing surface reflectivity. This particular incident angle is called the SPR angle, which depends on the wavelength of the incident light. At the SPR angle, the resonance is extremely sensitive to changes in the refractive index of the medium adjacent to the metal surface. These changes can be monitored by checking the intensity of the reflected light in real time, enabling precise measurements of thin film properties, as well as the surface molecular interactions.

A typical SPR instrument includes a flow cell with a slide and a monitoring system. The first group of interactants, called the ligands, are fixed onto a dextran-coated gold surface of the slide. The second interactant, called the analyte, is then injected through the flow cell and traverses the surface of the slide. The intensity of light reflected off the slide surface is affected by the

mass concentration of components at the liquid-surface interface. The interaction of the soluble analyte with the immobilized ligands is observed directly and continuously. The biomolecule interaction analysis is performed in real time, but the measurements can be also recorded as videos for later verification. The collected SPR measurements contain information on the kinetic rate and equilibrium binding constants for the interaction under investigation.

B. SPR sensorgram fitting

Fig 1 shows the SPR curve of a typical bioaffinity interaction experiment. In the association phase, the analyte is binding to the ligand, and the light intensity reflected off the binding site increases until it reaches the equilibrium phase, where the binding is saturated and the light intensity is maximized. In the disassociation phase, there is no more analyte in the flow, and the already-bound ligand and analyte dissociate from each other. The experiment ends by rinsing the analyte using a cleaning liquid prior to testing the next sample.

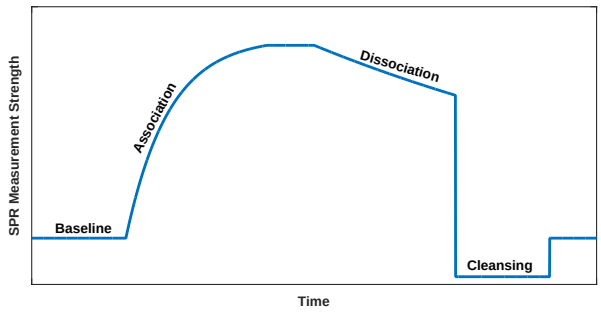

Fig. 1: Typical SPR curve

The sensorgram is fit to a kinetic model to compute the kinetic constants that characterize the interactions between molecules in SPR analysis. The most commonly used binding model for SPR biosensors is the Langmuir model [14]. It describes a 1:1 interaction in which one ligand molecule interacts with one analyte molecule. In theory, the formation of the ligand-analyte complex follows second-order kinetics. However, because the majority of SPR biosensors are fluidics-based and capable of maintaining a constant analyte concentration in a continuous liquid flow, the complex formation actually follows pseudo first-order kinetics [14]. This model assumes that the binding reactions are equivalent and independent at all binding sites and that the reaction rate is not limited by mass transport. Many interactions adhere to this model, in which the interaction is described by

$$A + B \underset{k_d}{\overset{k_a}{\rightleftarrows}} AB \tag{1}$$

where B represents the ligand and A the analyte. The rate of complex formation is represented by the association constant (k_a, in the unit of $M^{-1}s^{-1}$) and the rate of complex decay is represented by the dissociation constant (k_d, in the unit of s^{-1}). Another equilibrium constant is a derived quantity, $K_D = k_d/k_a$ (in the unit of M).

In the association phase, binding is measured as the analyte solution flows over the ligand surface. The sensorgram in the association phase examines the rate of complex formation. The measurement strength is observed to increase over time as the complex forms on the chip surface. The equations (2) to (6) illustrate the derivation of the association equation [14], where R_t is the signal level reflecting the mass of the compound $[AB]$.

$$[A]_t = \textbf{constant}[A] \tag{2}$$

$$[B]_t = [B]_{\textbf{max}} - [AB]_t \tag{3}$$

$$\because \frac{d[AB]_t}{dt} = k_a[A]_t[B]_t - k_d[AB]_t \tag{4}$$

$$\therefore \frac{dR_t}{dt} = k_a[A](R_{\textbf{max}} - R_t) - k_d R_t \tag{5}$$

$$\therefore R_t = \frac{R_{\textbf{max}}[A]}{K_D + [A]}\left[1 - e^{-(k_a[A]+k_d)t}\right] \tag{6}$$

In the dissociation phase, the analyte introduced in the carrier liquid is suddenly stopped. The rate of complex dissociation follows simple exponential decay described by first-order kinetics. The dissociation equation describes the time needed to reach a certain response level during the dissociation phase. This derivation is shown in equations (7) to (11), where R_0 is the signal level at the end of association [14], and at the beginning of dissociation.

$$\frac{d[AB]}{dt} = k_a[A]_t[B]_t - k_d[AB]_t \tag{7}$$

$$[A]_t = 0 \tag{8}$$

$$\therefore \frac{d[AB]}{dt} = -k_d[AB]_t \tag{9}$$

$$\therefore \frac{d[AB]}{dt} = -k_d R_t \tag{10}$$

$$\therefore R_t = R_0 e^{-k_d t} \tag{11}$$

Equations (6) and (11) are the association and dissociation models used later in parameter estimation.

C. System overview

The flow chart of the entire SPR data processing procedure is shown in Fig 2. Section III explains the details in the first two blocks on data pre-processing and automatic ROI detection. Section IV explains the last block on optimized kinetics parameter estimation.

III. ROI DETECTION

Raw data analyzed in this paper was a video captured by PlexArray System, and provided by its manufacturer, Plexera®. The system setup follows the prototype developed by Kretchmann [15], desorption is done about once a week, and sanitization is done about once a month, to ensure the cleanness of the system. In our experiment, the ligand was planted in an array as shown in Fig 3. The analyte, Human Immunoglobulin G, passed through the flow cell. The rows and columns of the binding sites were indexed, so that their locations could be referred to later. In our study, columns 1, 2, 11, and 12 contain data of interest, while other columns are for reference purposes only.

A. Pre-processing of the video data generated by the SPR machine

Images obtained using SPR are usually dark. The lack of contrast between the elliptical ROIs and the background makes the ROI detection difficult. Histogram Equalization (HE) is an effective method to achieve a wide dynamic range and improve the image contrast. Suppose the probability of intensity level r_k in a digital image is approximated by

$$p_r(r_k) = \frac{n_k}{MN}, \quad k = 0, 1, 2, \ldots, L-1 \tag{12}$$

where M and N are the row number and column number of the image, respectively, n_k is the number of pixels that have intensity r_k, and L is the number of possible intensity levels in the image. Then the histogram equalized intensity level is defined as

$$s_k = T(r_k) = (L-1)\sum_{j=0}^{k} p_r(r_j) = \frac{L-1}{MN}\sum_{j=0}^{k} n_j, \tag{13}$$

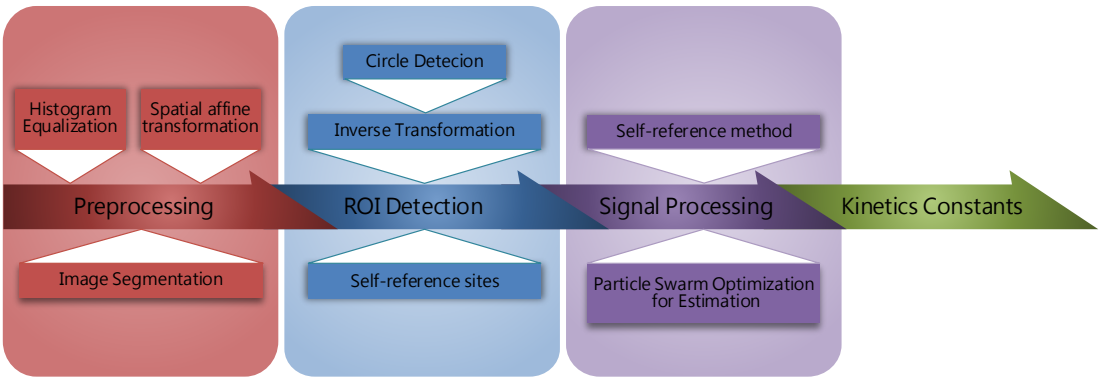

Fig. 2: Procedure to process the video and estimate the molecule binding parameters automatically.

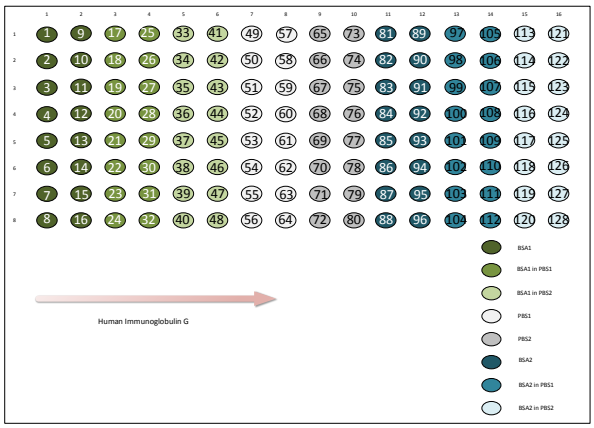

Fig. 3: SPR experiment illustration

with $k = 0, 1, 2, \ldots, L-1$, which approaches a uniform distribution that spans the entire dynamic range. Using HE, each pixel in the input image with intensity r_k is mapped to a corresponding pixel with level s_k in the output image. The original cropped image having an intensity histogram that spans a small range was mapped using HE to obtain the HE image having a much broader intensity histogram.

In an SPR experiment, usually the shape of the spots on the chip is circular. However, image deformation in the camera system distorts these circles into ellipses. In order to facilitate the ROI detection, we apply an affine transformation that scales the image and recovers the circular shape of the ROIs.

Circle detection is more efficient than ellipse detection in computational cost, and the affine transformation is a cost effective way to convert ellipse detection to circle detection.

The general affine transformation for pixel locations is defined by

$$\begin{bmatrix} x & y & 1 \end{bmatrix} = \begin{bmatrix} v & w & 1 \end{bmatrix} T = \begin{bmatrix} v & w & 1 \end{bmatrix} \begin{bmatrix} t_{11} & t_{12} & 0 \\ t_{21} & t_{22} & 0 \\ t_{31} & t_{32} & 1 \end{bmatrix} \quad (14)$$

where $[x, y]$ are the pixel coordinates in the output image, and $[v, w]$ are the pixel coordinates in the input image. In our experiment, the T matrix was empirically set to

$$T = \begin{bmatrix} 1 & 0 & 0 \\ 0 & 1.7 & 0 \\ 0 & 0 & 1 \end{bmatrix} \quad (15)$$

Applying the affine transformation to yield a scaled image with circular ROIs.

After the ROIs were identified in the transformed domain, we applied an inverse affine transform to convert the pixel locations within the ROIs back to the original image and extracted the exact gray level values from the original image.

B. Randomized Hough Transform for circle detection

The randomized Hough transform (RHT) [16], [17], [18] was used to detect the circular ROIs in the preprocessed images. Binding sites often have different brightness values, making a global threshold selection for circle detection challenging. Circle detection accuracy was improved by segmenting the image based on the groups of the ligands prior to performing ROI detection (Fig 4).

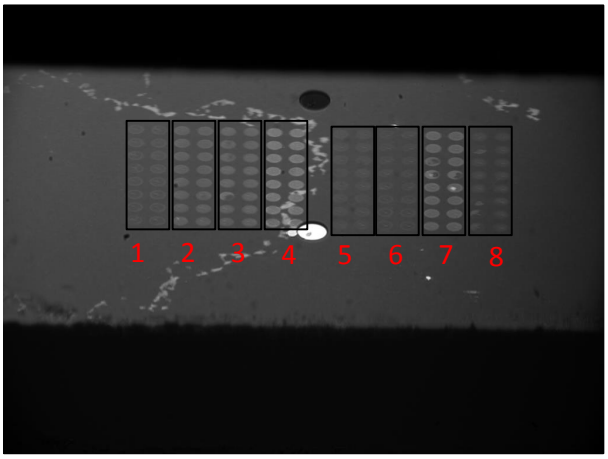

Fig. 4: Frame image segmentation

The RHT requires several user-defined parameters to control the execution of the algorithm. These parameters are listed below.

- **The validating threshold, v. The RHT accumulates votes through random sampling of a relatively small number of points in the circle parameter space. Once a circle parameter point gets at least v votes, the existence of the corresponding circle is verified in a verification phase of the algorithm. In verification, the whole circle is constructed, and the exact number of edge points on the circle is counted. Typically v is a small integer with a value of 2 or 3.**
- **The circle percentage threshold, p. The RHT does not expect to find a perfect circle. Instead, if there are enough**

points on a candidate circle, the RHT reports it as a real circle. This is not only reasonable but also necessary, because there are many factors that distort or damage parts of the circular pattern in the edge map. Such factors include the quantization error of the imaging, failure of the edge detection process to extract weak or blurred object boundaries, and the existence of other random noise. In the standard RHT, p is set as the required number of points on a circle: if a candidate circle is verified to have at least n_c points on it, then the circle will be reported as a real circle. However, a more reasonable form is to define p as the ratio of n_c to the circumference of the candidate circle. For example, setting $p = 0.7$, a candidate circle is identified as real if 70 percent of the circle is present on the edge map.

- **The maximum number of sampling, T. The RHT terminates its circle searching when no circle is detected after running T samplings.**

The RHT algorithm is summarized with the following steps and a flow chart (Fig 5).

Step 1: **Initialize a counter variable $t = 0$, which stores the number of unsuccessful samplings in the current sampling run.**

Step 2: **Generate a binary edge map using the Canny edge detector (although the choice of the edge detector can be flexible, the Canny edge detector is optimal in generating the edge map for natural images, and hence often adopted [19]). Randomly select three edge points from the binary edge map. This selection step is called a sampling. If these points are collinear, they cannot define a circle, thus the sampling fails. Set $t = t + 1$. Otherwise a circle with a center at (x, y) and a radius of r can be computed. The circle parameters (x, y, r) form a point in the parameter space.**

Step 3: **Store the parameter set, (x, y, r), into a hash table and set a vote count for it. The count is initialized to 1. If the parameter set is already in the hash table, increase its vote count by 1.**

Step 4: **If the parameter set gets more votes than the validating threshold v, the corresponding candidate circle is verified, and the number of edge points on the candidate circle is counted and stored in n_c. Then the ratio $p_c = \frac{n_c}{2\pi r}$ is calculated. If p_c is greater than or equal to the circle percentage threshold p, the candidate is recorded as a real circle in the edge image. The points on the identified circle are erased from the edge image, the hash table is emptied, and the counter variable t is reset to 0.**

Step 5: **If no circle is detected based on the three random edge points, set $t = t + 1$, and resample the edge points from Step 2. When t reaches the maximum sampling threshold T, the algorithm halts, and the detected circle parameters are reported.**

An example of the RHT process is illustrated in Fig 6. The figure shows how the green circles, determined by three randomly chosen points, gradually converge to the correct ROIs. After circular ROI detection by RHT, the coordinates of the pixels within the ROI are inverse-transformed back onto the original image. It is observed that the automatically detected ROI in the original image is accurate and these original pixel values can be used later for kinetics parameter estimation.

C. Self-referencing method

A self referencing method was adopted the to eliminate long-term drift that affects the whole image during measurement. This long-term drift may be caused by factors such as fluctuations

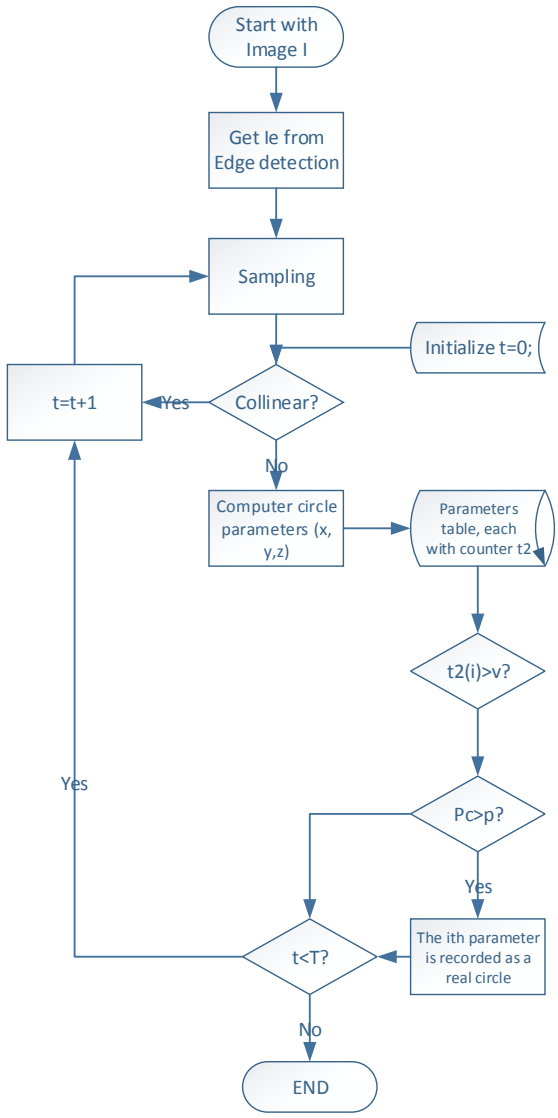

Fig. 5: RHT procedures

of the light source or changes in ambient temperature. First, four satellite spots were selected for each ROI at the following locations.

$$\begin{bmatrix} x_1 & y_1 \\ x_2 & y_2 \\ x_3 & y_3 \\ x_4 & y_4 \end{bmatrix} = \begin{bmatrix} x_0 - r_0 & y_0 - r_0 \\ x_0 - r_0 & y_0 + r_0 \\ x_0 + r_0 & y_0 - r_0 \\ x_0 + r_0 & y_0 + r_0 \end{bmatrix} \tag{16}$$

where $[x_0,\ y_0,\ r_0]$ are the center coordinates and radius of a particular ROI in anlaysis. The four satellite sites around the ROI are $[x_j,\ y_j]$ with $j = 1, \ldots, 4$. Some satellite spots contained a bubble or other factor that resulted in a drastic change in gray level value of the pixels. The decision to include a satellite in the analysis was made by comparing its value to that of the other satellites. The decision to include a satellite (P_j to be either true,

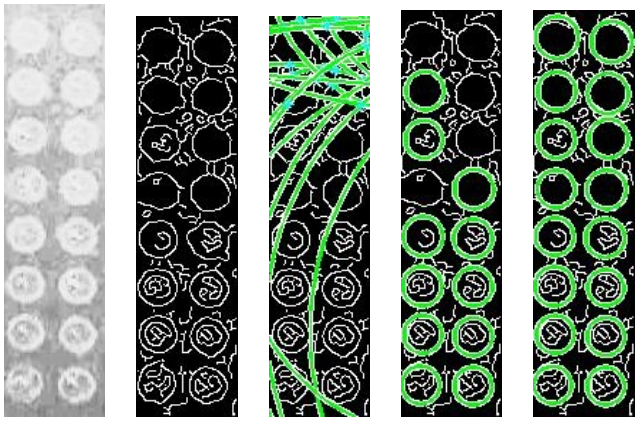

(a) (b) (c) (d) (e)

Fig. 6: An example run of RHT: (a) segmented image; (b) edge detection result; (c) circles, each consisting of three randomly picked points that are non-collinear; (d) gradual converging to ROI; (e) the final RHT result

1**, or false,** 0**) is defined by**

$$P_j = \begin{cases} 0 & \textbf{if } \sigma_j/\sigma_{j'} \geq \tau \\ 1 & \textbf{otherwise} \end{cases} \tag{17}$$

where σ_j is the variance of all four satellites; $\sigma_{j'}$ is the variance of three other satellites, and τ is a threshold. We used the average pixel gray level values of the satellite set as the reference to obtain a normalized SPR intensity curve over time,

$$I_{\textbf{normalized}} = I_{\textbf{signal}} - \bar{I}_{\textbf{satellites}} \tag{18}$$

where $I_{\textbf{signal}}$ denotes the the original measured intensity in each frame over time, and $I_{\textbf{normalized}}$ is the normalized signal. The average satellite intensity ($\bar{I}_{\textbf{satellites}}$) is given by

$$\bar{I}_{\textbf{satellites}} = \frac{\Sigma I_{s_i} \times P_i}{\Sigma P_i} \tag{19}$$

where ΣI_{s_i} is the light intensity of ith satellite in a satellite set.

Fig 7 shows the self-referencing result for spot 1. The black normalized curve, used to estimate the molecule binding parameters, was obtained by subtracting the red satellite reference intensity curve from the blue original intensity curve. Note that, in Fig 7, there were three cycles in this experiment, each with different signal intensities. Each cycle resulted from the analyte having a different concentration. The higher the concentration, the stronger the binding, the heavier the mass, and hence the greater the SPR measurement.

IV. Molecule Binding Parameters Estimation

Upon completion of automatic ROI detection from the recorded video, the SPR data were extracted and the kinetics constants estimated. These parameters were obtained using optimization algorithms that by minimized the MSE between the measurements and system model.

A. Particle swarm optimization algorithm

PSO was first proposed by Eberhart and Kennedy[20] and used for optimization of continuous nonlinear functions. It was designed to emulate the social behavior of a swarm. The swarm in PSO is composed of volume-less particles that move around solution space, each of which represents a feasible solution to the problem.

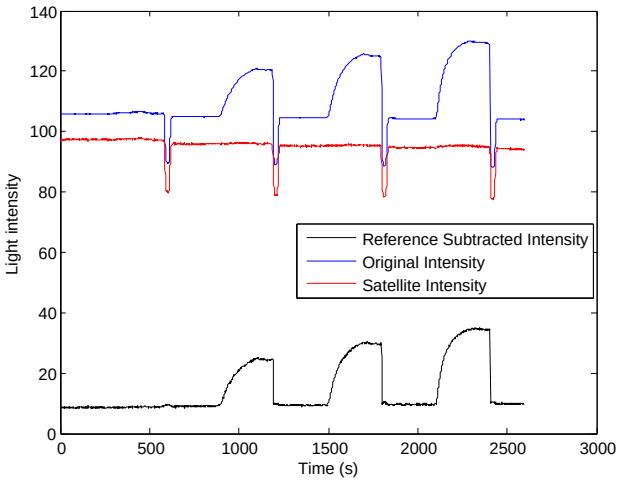

Fig. 7: Self-referencing result of spot 1

The PSO algorithm is summarized in the pseudo code, Algorithm 1.

Algorithm 1 PSO algorithm

Require: Random initial position and velocity of the particles: $\overrightarrow{X_i}(0)$ and $\overrightarrow{V_i}(0)$

```
while terminating condition is not reached do
    for i = 1 to number of particles do
        Evaluate the fitness← f(X_i)
        Update p_i and g_i
        Adapt velocity of the particle using equation 20 and 21
        Update the position of the particle;
return
```

PSO starts with a population of particles initialized with random positions marked by vector $\overrightarrow{x_i}$ and random velocities $\overrightarrow{v_i}$. The population of these particles is called a "swarm". Each particle P stores two state variables: its current position $\overrightarrow{x(t)}$ and its current velocity $\overrightarrow{v(t)}$. It is also equipped with a small memory comprising its previous best position $\overrightarrow{p(t)}$, i.e., the personal best experience and the best $\overrightarrow{p(t)}$ of all P's, $\overrightarrow{g(t)}$, i.e., the best position found so far in the population of the swarm.

Initially, $\overrightarrow{p(t)}$ and $\overrightarrow{g(t)}$ are set as $\overrightarrow{p(t)}$ = $\overrightarrow{g(t)}$ = $\overrightarrow{x(0)}$ for all particles. Once the particles are all initialized, iterations begin, where the positions and velocities of all the particles are altered by the following recursive equations (20) and (21). The equations are presented for the dth dimension of the position and velocity of the ith particle.

$$v_{id}(t+1) = \omega v_{id}(t) + c_1\varphi_1(p_{id}(t) - x_{id}(t)) + c_2\varphi_2(g_{id}(t) - x_{id}(t)) \tag{20}$$

$$x_{id}(t+1) = x_{id}(t) + v_{id}(t+1) \tag{21}$$

where ω is an inertia weight factor; $0 \leq \varphi_1, \varphi_2 \leq 2$ are two uniformly distributed random numbers in velocity update; c_1 and c_2 are two constant multiplier terms as the weights of "self cognitive awareness" and "social influence", respectively.

The first term in the velocity update rule represents the inertia of the particle. Since the coefficient c_1 has a contribution towards the self-exploration (or experience) of a particle, we regard it as

the particle's self-confidence. On the other hand, the coefficient c_2 weights the contribution towards motion of the particles in global best's direction, which takes into account the motion of all the particles in the preceding iterations. After calculating the velocities and positions of the particles at the next time step, $t+1$, the first iteration of the algorithm is completed. Typically, this process is iterated a certain number of time steps, or until an acceptable solution has been found, or until an upper limit of CPU usage has been reached.

B. Application of PSO to find binding parameters in SPR

In order to apply the PSO algorithm to find kinetic binding constants in SPR, we first defined the solution space as the possible range of the k_a and k_d. R_{max}, a scaling factor adapted to the specific video frame intensity values, was defined in equation (6). The fitness function was defined as the MSE between the parametric curve using estimated kinetic constants and the measured sensorgram data. The PSO was performed and the iteration stopped when it reached the stopping criteria based on total iteration number and the convergence of the MSE value.

V. RESULTS

Fig 3 in section III-A shows the SPR experiment layout of the ligants used in this study. Eight sets of ligands were planted on the chip prior to injecting the analyte. Each ligand type was arranged on the chip surface in an array consisting of 8 rows and 2 columns (Table I). The analyte consists of Human Immunoglobulin G (HIgG) in three different concentrations (Table II). The ROI spots were labeled by numerical indices as shown in Fig 3, and the analysis results on these ROIs will be referred to by these indices hereafter.

TABLE I: Ligands List

1-16	Bovine Serum Albumin (BSA) 1
17-32	BSA 1 in PBS 1
33-48	BSA 1 in PBS 2
49-64	Phosphate-buffered Saline (PBS) 1
65-80	Phosphate-buffered Saline (PBS) 2
81-96	Bovine Serum Albumin (BSA) 2
97-112	BSA 1 in PBS 1
113-128	BSA 2 in PBS 2

TABLE II: Analyte List

1	HIgG, 1.67×10^{-7}(M)
2	HIgG, 3.33×10^{-7}(M)
3	HIgG, 6.67×10^{-7}(M)

BSA1 and BSA2 (spot 1-16 and spot 81-96) were active ligands that interacted with the analyte. The other ligands were for reference only. The sensorgram curve was extracted by the procedures below.

A. ROI auto-detection result

Fig 8 shows the detected ROIs and the satellite sites around the ROI. It was observed that all the ROIs on the chip surface were correctly identified. Furthermore, the pixels inside each ROI were accurately identified, which was a crucial step for the subsequent estimation task.

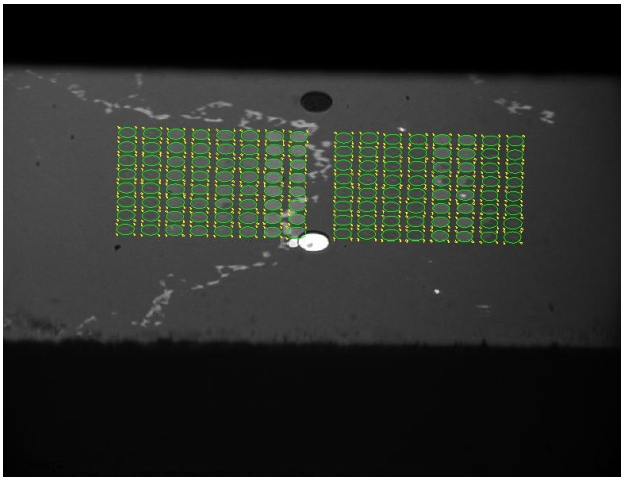

Fig. 8: Detection of ROI and its satellites

B. Kinetic constant estimation and fitting results for spot 1

In order to demonstrate the results in detail, we used spot 1 to show the kinetic constant fitting for an active spot. The other spots were processed in a similar manner, and the results for all the spots are presented in section V-C.

The sensorgram curve of spot 1 was shown previously in Fig 7, where three cycles with different analyte concentration were clearly visible. Fig 9 (a) to 9 (c) show the LM and PSO curve fitting results for the three cycles of spot 1. Since the three cycles share the same kinetic constants k_a and k_d, the MSE was evaluated as the summation of MSE across all three cycles. Using either LM or PSO, the estimated orders of magnitude of k_a or k_d were similar. PSO is a random searching algorithm and hence 100 Monte Carlo simulation runs were carried out. The range of the estimated parameters, as well as MSE values, are also reported in Fig 9. It was observed that PSO consistently yielded a smaller MSE value than the LM algorithm. Based on the Monte Carlo simulation results of our PSO algorithm, we can deduce that the solution space of this project is highly nonlinear with many local minima. This conclusion was made because the best result with the minimum MSE was not always found within the 100 Monte Carlo simulations, although the solutions were still very good and much better than the solution found using the LM algorithm. PSO achieved better result than LM because the LM algorithm is a gradient based approach that is sensitive to local minima which limits its ability to solve non-linear problems.

C. MSE comparison between LM fitting and PSO fitting for all the spots

The results for all of the other active spots were similar to spot 1 that was described in detail in section V-B. The estimated molecular binding parameters and the MSE are shown using both the LM and PSO methods (Table III). The MSE values for all the active ROI spots are plotted in Fig 10 for easy comparison. The PSO fitting algorithm was consistently found to be more accurate than the commercially used LM algorithm. Out of 100 Monte Carlo simulations, the decrease in MSE (an improvement) by PSO over LM was at least 16.58% and up to as much as 73.9%.

D. Kinetic constant estimation and fitting results for tainted data

Spots 88 and 96 were affected by air bubbles in the flow cell. As a result, some cycles of the sensorgrams were invalid. Given

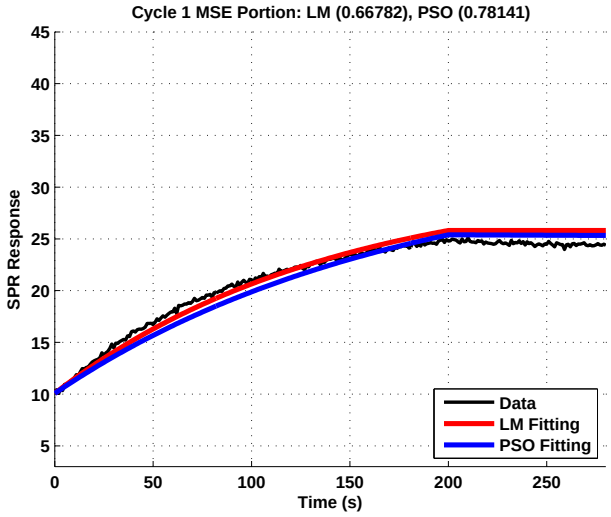

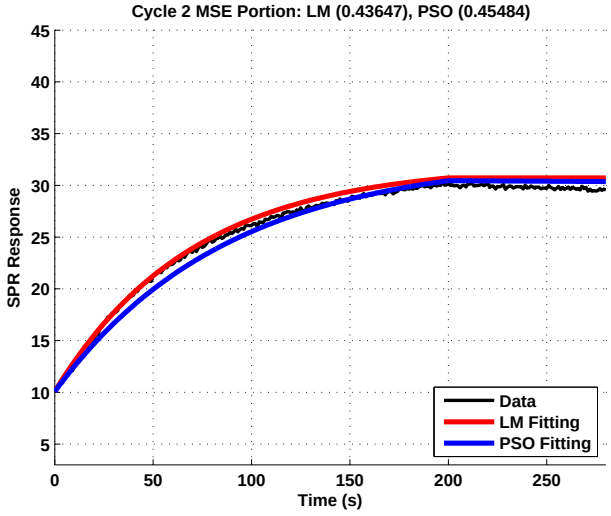

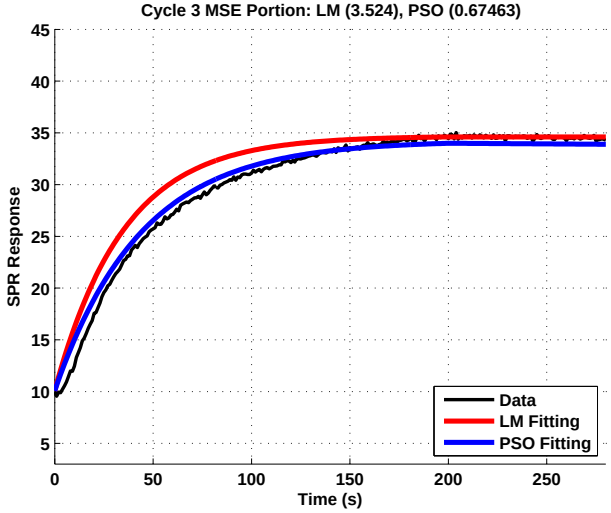

	$k_a(s^{-1}M^{-1})$	$k_d(s^{-1})$	MSE
LM	4.2900×10^4	0	4.6283
PSO best	3.4211×10^4	5.1457×10^{-5}	1.9109

$3.4211 \times 10^4 < k_a < 3.4469 \times 10^4$
$0 < k_d < 5.1457 \times 10^{-5}$
$1.9109 < \text{MSE} < 1.9455$

Fig. 9: PSO curve fitting result for spot 1

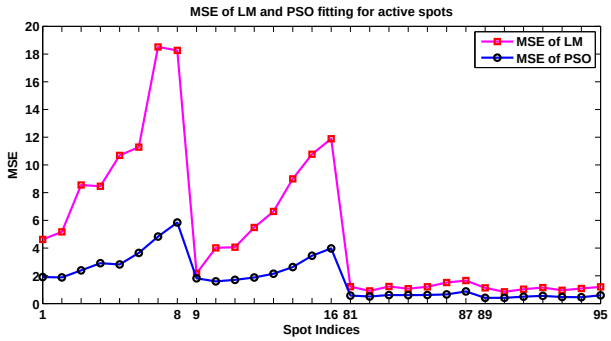

Fig. 10: MSE comparison between LM and PSO fitting on all the active ROI spots

the less reliable data, the results on these two noisy spots are excluded from comparison.

VI. Conclusion and Future Work

This paper presented new image processing methods to enhance the efficiency of surface plasmon resonance. The first enhancement was a method to automatically detect the regions of interest (ROI). Automatic ROI detection was achieved using image histogram equalization, affine transform, edge detection, and the Randomized Hough Transformation. Applying the combination of these techniques successfully identified the pixels inside the ROIs for data extraction. The second enhancement was an improved method to estimate the molecule binding parameters. A self-referencing method was used to mitigate the effect of long term baseline shift and other noise. In addition, image intensity data within each ROIs were analyzed using particle swarm optimization to find the molecule binding parameters. The PSO algorithm is more effective at analyzing nonlinear systems than the LM algorithm that used a gradient approach. As a result, the PSO algorithm had better fitting accuracy between the model and the data, consistently yielding a smaller mean squared error than the current LM method.

Future work includes: *(1)* Refining each method to further improve the detection efficiency for better performance in real-time applications, *(2)* Collecting real-time data from more experiments to verify the robustness of the new ROI detection and parameter estimation methods.

Acknowledgment

The authors thank Plexera®LLC for providing the SPR measurement data.

References

[1] M. Malmqvist and R. Karlsson, "Biomolecular interaction analysis: affinity biosensor technologies for functional analysis of proteins," in *Current Opinion in Chemical Biology*, February 2002, pp. 378–383.

[2] R. Copeland, D. Pompliano, and T. Meek., "Drug-target residence time and its implications for lead optimization," in *Nat Rev Drug Discov*, September 2002, pp. 730–739.

[3] R. Glaser. and G. Hausdorf, "Binding kinetics of an antibody against HIV p24 core protein measured with real-time biomolecular interaction analysis suggest a slow conformational change in antigen p24," in *Journal of Immunological Methods*, September 1996, pp. 1–14.

[4] S. Salapaka and M. Salapaka, "Scanning probe microscopy," *Control Systems, IEEE*, vol. 28, no. 2, pp. 65–83, April 2008.

[5] B. Redlich, "Infrared spectroscopy of (bio)molecules in the gas phase using the free-electron-laser 'felix'," in *Infrared and Millimeter Waves and 13th International Conference on Terahertz Electronics, 2005. IRMMW-THz 2005. The Joint 30th International Conference on*, vol. 1, Sept 2005, pp. 307–308 vol. 1.

	LM			PSO		
Spot	k_a	k_d	MSE	k_a	k_d	MSE
1	4.2900×10^4	0	4.6283	3.4211×10^4	5.1457×10^{-5}	1.9109
2	4.1600×10^4	0	5.1734	3.2236×10^4	7.8155×10^{-5}	1.8845
3	4.7400×10^4	0	8.5518	3.3677×10^4	6.8332×10^{-5}	2.3899
4	4.8800×10^4	0	8.4644	3.5122×10^4	7.7952×10^{-5}	2.9143
5	4.4100×10^4	0	10.6897	3.0690×10^4	4.9807×10^{-5}	2.8205
6	4.5200×10^4	0	11.2869	3.1773×10^4	5.4298×10^{-5}	3.6504
7	4.9600×10^4	0	18.5110	3.2335×10^4	6.2582×10^{-5}	4.8308
8	4.7200×10^4	0	18.2665	3.1914×10^4	6.6521×10^{-5}	5.8437
9	3.8200×10^4	0	2.1794	3.9394×10^4	7.5838×10^{-5}	1.8181
10	4.0000×10^4	0	4.0172	3.3308×10^4	6.5380×10^{-5}	1.5995
11	4.0500×10^4	0	4.0637	3.3085×10^4	8.3508×10^{-5}	1.7088
12	4.2400×10^4	0	5.4863	3.2648×10^4	7.3786×10^{-5}	1.8776
13	4.3200×10^4	0	6.6458	3.2797×10^4	5.8035×10^{-5}	2.1497
14	4.4200×10^4	0	8.9908	3.2292×10^4	5.2531×10^{-5}	2.6341
15	4.5300×10^4	0	10.7705	3.3166×10^4	6.7892×10^{-5}	3.4486
16	4.5500×10^4	0	11.8910	3.2913×10^4	6.6027×10^{-5}	3.9762
81	3.9300×10^4	0	1.2178	5.3109×10^4	8.3513×10^{-5}	0.5733
82	4.0000×10^4	0	0.9118	4.8966×10^4	8.5889×10^{-5}	0.5117
83	3.8100×10^4	0	1.2309	4.8692×10^4	7.1950×10^{-5}	0.6149
84	3.7800×10^4	0	1.0766	4.7274×10^4	7.4515×10^{-5}	0.6058
85	3.6900×10^4	0	1.2125	4.6796×10^4	6.5092×10^{-5}	0.6204
86	3.3100×10^4	0	1.5157	4.3628×10^4	7.0387×10^{-5}	0.6619
87	3.6300×10^4	0	1.6559	4.4077×10^4	9.1886×10^{-5}	0.8707
89	3.6100×10^4	0	1.1302	5.0284×10^4	6.0331×10^{-5}	0.4134
90	3.8100×10^4	0	0.8470	4.9719×10^4	6.3409×10^{-5}	0.4091
91	3.8000×10^4	0	1.0342	4.8193×10^4	8.2558×10^{-5}	0.4951
92	3.7600×10^4	0	1.1500	4.8336×10^4	5.5014×10^{-5}	0.5566
93	3.6500×10^4	0	0.9602	4.5642×10^4	5.8846×10^{-5}	0.4696
94	3.3700×10^4	0	1.0884	4.4378×10^4	6.7123×10^{-5}	0.4608
95	3.4400×10^4	0	1.2054	4.2790×10^4	7.9544×10^{-5}	0.5909

TABLE III: Parameter estimation and MSE comparison between LM and PSO fitting on all the active ROI spots

[6] **Y. Kolesnikov, M. Kabakova, A. Novikov, E. Thiel, and V. Zemskii, "Spectral gas sensitivity of immobilized ph-indicator molecules," in *Lasers and Electro-Optics Europe, 2003 Conference on*, June 2003, p. 498.**

[7] **B. Liedberg, C. Nylander, and I. Lunström, "Zeitschrift für physik," *Sens. Actuators*, vol. 4, pp. 299–340, 1983.**

[8] **J. Homola, "Surface plasmon resonance sensors for detection of chemical and biological species," *Chem. Rev.*, vol. 108, no. 2, pp. 462–493, 2008.**

[9] **M. Piliarik, L.Parova, and J.Homola, "High-throughput SPR sensor for food safety," *Biosens. Bioelectron*, vol. 24, no. 5, pp. 1399–1404, 2009.**

[10] **D. Shankaran, K.V.Gobi, and N.Miura, "Recent advancements in surface plasmon resonance immunosensors for detection of small molecules of biomedical, food and environmental interest," *Sens. Actuat. B. Chem*, vol. 121, no. 1, pp. 158–177, 2007.**

[11] **R. Nejm, M. Hussein, and A. Ayesh, "A study of the surface plasmon enhancement using ARC on thin film si solar cell performance," in *High Capacity Optical Networks and Enabling Technologies (HONET-CNS), 2013 10th International Conference on*, Dec 2013, pp. 51–55.**

[12] **Y. Xu, X. Ma, and H. Zhao, "A novel design of distributed surface plasmon sensors based on nanoparticles composite layers," in *Biophotonics, Nanophotonics and Metamaterials, 2006. Metamaterials 2006. International Symposium on*, Oct 2006, pp. 310–313.**

[13] **W. Yuan, H. Ho, C. Wong, S. Wu, Y. Suen, S. Kong, and C. Lin, "Sensitivity enhancement of phase-sensitive surface plasmon resonance biosensor using multi-pass interferometry," in *Biophotonics, Nanophotonics and Metamaterials, 2006. Metamaterials 2006. International Symposium on*, Oct 2006, pp. 202–205.**

[14] **R. Luo, *Protein interaction analysis*, 1st ed. USA: Bio-Rad Laboratories, Inc., 2013, no. Bulletin 6300.**

[15] **K. Erika, *Handbook of Biosensors and Electronic Noises: Medicine, Food, and the Environment*, 1st ed. USA: CRC Press, 1996.**

[16] **H. Yuen, J. Princen, J. Illingworth, and J. Kittler, "Comparative study of hough transform methods for circle finding," *Image and Vision Computing*, vol. 8, no. 1, pp. 71 – 77, 1990. [Online]. Available: http://www.sciencedirect.com/science/article/pii/026288569090059E**

[17] **P. Kultanen, L. Xu, and E. Oja, "Randomized hough transform (rht)," in *Pattern Recognition, 1990. Proceedings., 10th International Conference on*, vol. i, Jun 1990, pp. 631–635 vol.1.**

[18] **L. Xu and E. Oja, "Randomized hough transform," *Encyclopedia of Artificial Intelligence*, pp. 1354–1361, 2008.**

[19] **J. Canny, "A computational approach to edge detection," *Pattern Analysis and Machine Intelligence, IEEE Transactions on*, vol. PAMI-8, no. 6, pp. 679–698, 1986.**

[20] **R. Eberhart and J. Kennedy, "A new optimizer using particle swarm theory," in *Micro Machine and Human Science, 1995. Proceedings of the Sixth International Symposium on*, Oct 1995, pp. 39–43.**